Large and projected strengthening moisture limitation on end-of-season photosynthesis

Yao Zhang[a,b,1], Nicholas C. Parazoo[c], A. Park Williams[d], Sha Zhou[a,d,e], and Pierre Gentine[a,e,1]

[a]Department of Earth and Environmental Engineering, Columbia University, New York, NY 10027; [b]Climate and Ecosystem Sciences Division, Lawrence Berkeley National Laboratory, Berkeley, CA 94720; [c]Jet Propulsion Laboratory, California Institute of Technology, Pasadena, CA 91109; [d]Lamont–Doherty Earth Observatory, Columbia University, Palisades, NY 10964; and [e]Earth Institute, Columbia University, New York, NY 10027

Edited by Christopher B. Field, Stanford University, Stanford, CA, and approved March 13, 2020 (received for review August 19, 2019)

Terrestrial photosynthesis is regulated by plant phenology and environmental conditions, both of which experienced substantial changes in recent decades. Unlike early-season photosynthesis, which is mostly driven by temperature or wet-season onset, late-season photosynthesis can be limited by several factors and the underlying mechanisms are less understood. Here, we analyze the temperature and water limitations on the ending date of photosynthesis (EOP), using data from both remote-sensing and flux tower-based measurements. We find a contrasting spatial pattern of temperature and water limitations on EOP. The threshold separating these is determined by the balance between energy availability and soil water supply. This coordinated temperature and moisture regulation can be explained by "law of minimum," i.e., as temperature limitation diminishes, higher soil water is needed to support increased vegetation activity, especially during the late growing season. Models project future warming and drying, especially during late season, both of which should further expand the water-limited regions, causing large variations and potential decreases in photosynthesis.

end of photosynthesis | solar induced fluorescence (SIF) | gross primary production (GPP) | climate change | water stress

Global change and human management have dramatically increased vegetation growing-season length and peak-season vegetation activity during the past several decades (1–4). The resultant greening of the Earth also increased the carbon uptake by terrestrial ecosystems, offsetting one-third of anthropogenic CO_2 emissions (5) and providing negative feedbacks to global warming (6). However, recent studies indicate emerging negative effects of warming on ecosystem carbon sequestration (7, 8), making it questionable whether the increase in terrestrial carbon uptake of the past several decades will continue. Vegetation photosynthesis, especially during the late growing season, has large variations and high sensitivity to different limiting resources and plays an important role in the global carbon cycle (9, 10). The prediction of late-season photosynthesis by Earth system models faces large uncertainty, as it is affected by conditions not only during the late growing season but also by legacy effects from previous seasons or years (11, 12). For example, if warming allows for earlier and more rapid vegetation growth in spring, this could draw down soil moisture, potentially resulting in a lagged adverse effect on plant photosynthesis in the late growing season (12, 13). Complex changes in vegetation dynamics such as changes in, and responses to, growing-season length are large sources of uncertainty in future projections of ecosystem carbon uptake and functioning, as the coupled relationship between vegetation and soil moisture is notoriously challenging to model (14, 15).

Compared with plant phenology derived from remotely sensed greenness indices, plant physiological phenology (i.e., phenology based on photosynthesis) is more sensitive to the environment due to the additional physiological regulation (16), as well as changes in leaf pigment concentration and canopy structure that are not effectively captured by the conventional normalized difference vegetation index (NDVI) (17, 18). Factors causing the variations of the late growing-season photosynthesis or ending date of photosynthesis (EOP) can therefore also be regarded as limiting factors to ecosystems productivity. Nutrients, photoperiod, and several other factors can also play a role in regulating physiological phenology, but they often act on longer time scales and are not considered here. Previous studies mostly focus on the effect of warming on phenology, especially in the northern middle to high latitude (9, 12). The effect of water limitation, however, is less well understood. Considering the global warming and potentially drying trend predicted by Earth system models, water limitation may become increasingly important as the temperature limitation diminishes (19).

Due to limited direct observations, especially of photosynthesis and soil moisture, quantifying the environmental limitations on EOP, when water resources can be limiting, has proven challenging (14). Successful retrievals of sun-induced chlorophyll fluorescence (SIF) from satellite observations now provide an effective way to observe plant photosynthesis at the global scale (20). SIF is emitted during the light reaction of photosynthesis and is strongly linked to the energy absorption by chlorophyll and successive partitioning to photochemical carbon fixation (21). Leaf- and canopy-level observations have revealed a strong and near-linear relationship between remotely sensed SIF and in situ ecosystem photosynthesis, especially at weekly to seasonal time scales (22). Here, we used a machine learning-reconstructed contiguous SIF (CSIF) (23) dataset as a proxy of ecosystem gross

Significance

Late-season photosynthesis on land contributes greatly to annual total carbon fixation and is sensitive to climate. It is generally agreed that temperature limitation on late-season photosynthesis will alleviate with warming, but the effects of water availability are highly uncertain. Here, we use satellite and in situ observations to show that water limitation on late-season photosynthesis is regulated by both soil water and mean annual temperature. Considering the predicted warming and soil drying over most of the land surface by Earth system models, water availability is expected to become increasingly important as a limiting factor for late-season photosynthesis and carbon uptake.

Author contributions: Y.Z. and P.G. designed research; Y.Z. performed research; Y.Z., N.C.P., A.P.W., S.Z., and P.G. analyzed data; and Y.Z., A.P.W., S.Z., and P.G. wrote the paper.

The authors declare no competing interest.

This article is a PNAS Direct Submission.

Data deposition: The data and code have been made available at GitHub, https://github.com/zhangyaonju/EndofSeasonPhotosynthesis.

[1]To whom correspondence may be addressed. Email: yaozhang@lbl.gov or pg2328@columbia.edu.

This article contains supporting information online at https://www.pnas.org/lookup/suppl/doi:10.1073/pnas.1914436117/-/DCSupplemental.

First published April 13, 2020.

primary production (GPP) to investigate the temperature and water limitations and their interactive effect on the EOP. The machine-learning algorithm is trained on more than 1.8 million paired samples from Orbiting Carbon Observatory 2 (OCO-2) level 2 SIF and colocated Moderate Resolution Imaging Spectroradiometer (MODIS) reflectance data during 2015 to 2016. This reconstructed CSIF dataset is demonstrated to well capture the interannual variability of OCO-2 SIF even for years without training samples, and has a global continuous coverage with high temporal frequency (4 d), low uncertainty, and a longer duration (starting in 2001) than the original product (for example, OCO-2 SIF has a 16-d revisit cycle, starting from October 2014) (*Methods* and *SI Appendix*, Text S1 and Fig. S1). Comparisons with site-level eddy-covariance observations demonstrate rather high accuracy in capturing the drought responses and spatial and interannual variability of EOP ($R = 0.96$ and 0.77 for all site-year and interannual anomalies, respectively; *SI Appendix*, Figs. S2 and S3). We also note that evergreen needleleaf forest has less-than-optimal performance as compared with other ecosystem types; this should have limited effects on our analysis and has been discussed in detail in *SI Appendix*, Text S1.

Results and Discussion

Precipitation and Temperature Limitations on EOP. We first derive EOP from CSIF based on a weighted spline-fit algorithm with a fixed per-pixel threshold (*Methods*); its correlations with average temperature and precipitation are then calculated for different preseason lengths (15, 30, 60, 90 d). The preseason is defined as a time period right before the multiyear average EOP. Fig. 1 shows the strongest EOP–climate correlation among these preseason lengths. EOP in both high-latitude and low-latitude cold regions (e.g., Qinghai Tibet Plateau) correlates positively with pre-EOP temperature and negatively with pre-EOP precipitation, i.e., higher temperature and lower precipitation correspond to delayed EOP. In low-latitude regions or arid ecosystems, the correlations are reversed. These relationships are robust regardless of the climate datasets used (European Centre for Medium-Range Weather Forecasts (ECMWF) Re-Analysis (ERA)-Interim or remote sensing-based; *Methods*) (Fig. 1). Similar patterns can

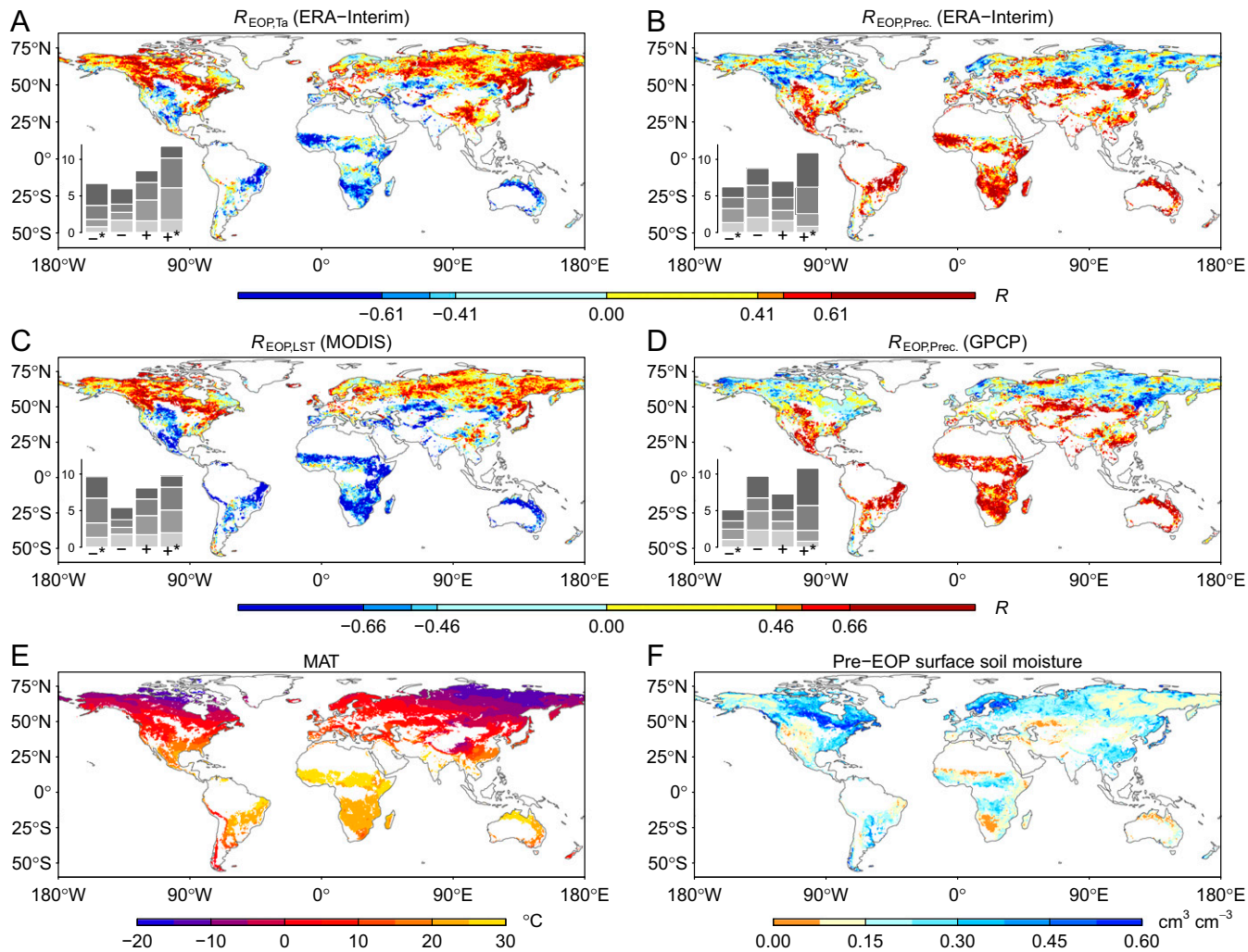

Fig. 1. Correlation between CSIF derived EOP and climate variables. (*A* and *B*) Correlation with ERA-Interim pre-EOP temperature and precipitation. (*C* and *D*) Correlation with pre-EOP mean daily LST from MODIS and precipitation from GPCP. The 0.1, 0.05, and 0.01 significance level of correlation correspond to ±0.41, ±0.48, and ±0.61 for ERA-Interim (2001 to 2017) and ±0.46, ±0.53, and ±0.66 for remote sensing-based datasets (2003 to 2016). Correlations are calculated for each climate variable with different preseason lengths (15, 30, 60, 90 d), and only the strongest correlation is shown for each pixel in the maps. *Insets* show the frequency of the preseason lengths for each correlation category ("−*," "−," "+," and "+*" for significant negative, negative, positive, and significant positive, respectively), with darker color indicating longer preseason length. (*E*) MAT from ERA-Interim during 2001 to 2017. (*F*) One-month pre-EOP average SSM from SMAP during 2015 to 2018. Cropland, tropical rainforest with weak seasonality, and barren area are masked and shown as white.

also be found if we use EOP derived from near-infrared reflectance of vegetation (NIR_V) instead of CSIF (*SI Appendix*, Text S2 and Fig. S4). We also calculate the partial correlations between CSIF-derived EOP and radiation, temperature, and precipitation, with the other variables fixed (*SI Appendix*, Fig. S5). The partial correlations are weaker than the simple correlations, but the spatial patterns are similar.

We regard the variables with positive correlations to be the limiting factors for ecosystem productivity in the late growing season, since for most cases, increase in these resources is beneficial. Temperature may negatively impact photosynthesis when it is above an optimal value, but the average and maximum (during extremely hot years) temperature during the pre-EOP are mostly below 25 °C (*SI Appendix*, Fig. S6), except for the Sahel region, where the dominating cropland and savannas ecosystems also have higher optimal temperature (24). The correlation between EOP and temperature ($R_{\mathrm{EOP,Ta\ or\ }R_{\mathrm{EOP,LST}}}$) is spatially inversely correlated with the correlation between EOP and precipitation ($R_{\mathrm{EOP,Prec}}$, $R = -0.60$ and -0.67, $P < 0.001$, for ERA-Interim and remote-sensing datasets, respectively; *SI Appendix*, Fig. S7). This suggests that EOP in most regions is either limited by temperature or water. Negative temperature effects can be mostly attributed to water limitation, as demonstrated below. For most pixels, temperature averaged over 1 to 2 mo pre-EOP has the strongest effect on EOP, while precipitation affects EOP with a longer pre-EOP period (2 to 3 mo) (Fig. 1 and *SI Appendix*, Fig. S8). This is due to the memory of soil moisture on subseasonal and seasonal time scales (25).

By comparing these correlations with the mean annual temperature (MAT) and 1-mo pre-EOP surface soil moisture (PSSM) retrieved from the Soil Moisture Active Passive (SMAP) satellite (26) (*Methods*), we find that the regions limited by precipitation (positive correlation with EOP) have either high MAT or low PSSM (Fig. 1). Although the surface soil moisture (SSM) retrieved from SMAP only represents the upper 5 centimeters of soil, observations at 6:00 AM local time may be strongly coupled to soil moisture at deeper depths due to plant hydraulic redistribution (27), especially in semiarid regions where water limitation can be important. A comparison between Gravity Recovery and Climate Experiment (GRACE) liquid water equivalent thickness (LWET) and SMAP SSM also demonstrates high spatiotemporal consistency for most low- to midlatitude regions (*SI Appendix*, Figs. S9 and S10), further supporting that SSM can correctly represent the water condition at deeper depth on monthly time scales. We also calculate PSSM with different preseason lengths and normalized using wilting point and soil porosity (*SI Appendix*, Figs. S11 and S12). These results show similar spatial patterns and do not change our main findings.

In the MAT and PSSM two-dimensional (2D) space, regions with significant positive and negative correlation with pre-EOP temperature can be effectively separated using a support vector machine (SVM) (Fig. 2*A*). SVM is a supervised classification algorithm that can find an optimum hyperplane (or line) to separate the labeled samples into different categories, so that the gap (or margin) between two classes is maximized (*Methods*). Because some regions are colimited by both water and temperature (MAT ~10 °C and PSSM between 0.2 and 0.3 $cm^3\ cm^{-3}$), the SVMs computed on either temperature or precipitation alone (green lines in Fig. 2 *A* and *B*) do not overlap with each other. However, we are able to find a third SVM only based on pixels whose EOP is limited by either water or temperature, i.e., EOP positively correlates with pre-EOP precipitation or temperature, respectively (*Methods*). This SVM function, relying on both MAT and PSSM, suggests that there is an interactive effect between ecosystem energy availability (as assessed by MAT) and soil water resource (as assessed by PSSM). Coordination of these two determines the limiting environmental factors to EOP. A very similar SVM can also be found using the NIR_V dataset (*SI Appendix*, Fig. S13). If we do not consider the interactive effect and instead use a combination of two independent thresholds for MAT and PSSM to separate the temperature and water limited area (*SI Appendix*, Text S5 and Fig. S14), the accuracy of the model prediction decreases, with a lower kappa coefficient (0.767 as compared to 0.825 for SVM, *SI Appendix*, Table S1). Previous studies attribute the differential responses to water availability as biome dependent, such as differences between grassland and forest (28, 29). We do find a biome dependence for this environmental limitation on EOP (Fig. 2*C*), but the predictability using biome type is lower compared to the SVM (accuracy and kappa coefficient decrease by 0.17 and 0.33, respectively), which is uniquely based on climatic conditions. This suggests that environmental factors can also play an important role in shaping the differential responses to water limitation, both through the direct effect on plant physiology, and indirect and interactive effect on biome distribution.

Evidence from EC Flux Measurements. To test whether this joint regulation of soil moisture and MAT also exists in field observations, we use 50 flux tower sites with at least 5 y of observations across the globe. Due to the limited number of sample sites, we do not attempt to fit another SVM for the flux-based measurements but we instead use the SVM obtained from remote sensing data. The SVM fitted from the remote sensing data performs well in separating the sites that are more limited by water (red) or temperature (blue) (Fig. 3). In the margin of the SVM, both temperature- and water-limited sites exist, and are aligned along the SVM function. Sites that are both (yellow) limited by water and temperature or neither (green) also mainly locate within the SVM's margin, with no clear biome type dependence. Outside the margin of the SVM, water-limited sites are dominated by grasslands and woodlands, while the temperature-limited sites are mostly forest. If we replace the SMAP-based PSSM with in situ soil moisture measurements, the clustering still exists, but the function that separates the water- and temperature-limitation changes (*SI Appendix*, Fig. S15). This is likely due to the low cross-site comparability of soil moisture caused by differences in soil properties (porosity, soil texture), which affect the relationship between soil moisture and water potential, as well as differences in measurement sensors and calibration, measurement depth, and periods of observation.

The interactive effect between energy and water can be explained by a supply versus demand perspective on resources. Energy is beneficial for plants' biochemical processes to fix carbon, but also increases evaporative demand, thus depleting soil water resources. For example, the potential for vegetation growth increases with MAT (*SI Appendix*, Fig. S16), suggesting that energy availability increases the upper boundary of the plant growth if water is not limiting. Several previous studies also suggest that a heatwave may not necessarily decrease vegetation photosynthesis and canopy greenness unless it is accompanied with low soil moisture (30, 31). However, greater plant biomass together with higher temperature also leads to greater water consumption in these regions, and a higher PSSM is needed to support vegetation water needs. Similar responses are also found for the temperature and precipitation regulation on interannual variation of NDVI (32). From a physiological perspective, lower soil moisture increases stomatal sensitivity to vapor pressure deficit (VPD) (33), which is largely dependent on temperature. Lower MAT (or VPD) has a smaller effect on stomatal closure, making plants less dependent on precipitation water supply in colder conditions. This mechanism is also supported by field experiments: at higher temperature, the decrease of soil moisture exerts stronger limits on stomatal conductance and photosynthesis for multiple boreal forest species (34). In addition, this interactive effect of MAT and PSSM can also be related to plant

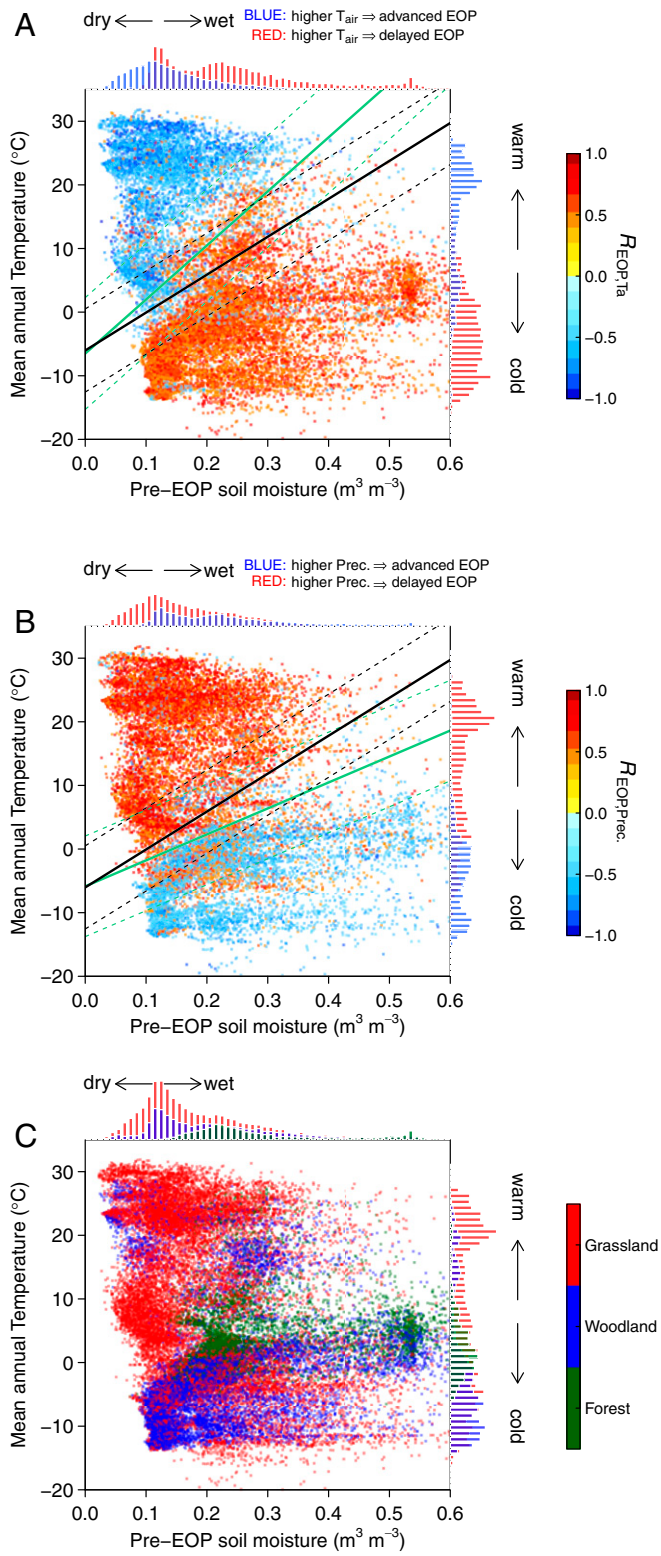

Fig. 2. Temperature and precipitation limitation on EOP in the MAT and PSSM space. Correlation between EOP and pre-EOP temperature (*A*) and precipitation (*B*) from ERA-Interim. Only pixels with significant relationship ($P < 0.1$) are shown. The green lines in *A* and *B* shows the separation of the positive and negative correlation. The black line separates the temperature- or precipitation-limited (positive correlation between EOP and pre-EOP air temperature [Ta] or precipitation [Prec.]) regions ($y = 59.60x - 6.03$). Dashed lines show the margins of the SVM. The dominate vegetation type for each 0.5° grid cell from MODIS is shown in *C*. The histograms on the top and right of the graphs shows the marginal distribution on PSSM and MAT, respectively. The landcover data are aggregated from IGBP classification. Grassland includes grassland, savannas, and wetland. Woodland includes open and closed shrubland, and woody savannas. Forest includes evergreen needleleaf forest, deciduous broadleaf forest, and mixed forest.

biogeography. Compared with grasslands, which are mostly distributed in warm and dry regions, forests tend to grow in cooler regions and generally have deeper roots, enabling access to deep soil water. These forests can therefore sustain photosynthesis under lower SSM for longer periods of time, and are more resistant to heatwaves or droughts (29). Although increasing CO_2 in the atmosphere can decrease stomatal conductance (35), this water-saving effect is strong only in regions and periods where transpiration dominates the water flux and can be almost cancelled out by the concurrent increase of VPD (36). Several free-air CO_2 enrichment experiments also suggest that increased CO_2 might not compensate for the drought-induced carbon losses (37, 38). Other factors (e.g., radiation, ozone) that may covary with temperature or precipitation can also trigger the leaf senescence and EOP, their effects should be further investigated.

Future Changes in Water Limitation on EOP. To evaluate the robustness of this SVM through time, we calculate temperature and water limited regions for two separate periods (2001 to 2009 and 2009 to 2017) and fitted two additional SVMs for each period. The SVMs for each period are almost identical to the SVM we find previously for the entire study period, and their classification performances are also comparable (*SI Appendix*, Fig. S17). This suggests that this energy and water colimitation on EOP holds through time and may be used for future predictions. We then predict the water-limited regions and their changes until 2100 using simulations from 23 climate models that took part in phase 5 of the Coupled Model Intercomparison Project (CMIP5), under both Representative Concentration Pathway (RCP) 4.5 and RCP8.5 scenarios (Fig. 4). Using the ensemble median of MAT and PSSM, the predictions of current water-limited regions are similar to our remote sensing-based observations, further corroborating the effectiveness of the SVM classification. Warming and drying in the future expand the water-limited regions under both RCP4.5 and RCP8.5 scenarios. This increase is much larger in RCP8.5 than in RCP4.5, with much of the boreal forests in Canada and Europe under water threat. The spread of this prediction across models is nonetheless large, ranging from ∼45 to 70% of the total land surface at the 2010s to ∼50 to 90% at the 2090s under RCP8.5. The Institut Pierre-Simon Laplace and Institute for Numerical Mathematics Climate Model Version 4 models predict the largest and smallest increase in water-limited area during the 21st century, respectively (*SI Appendix*, Fig. S18).

Most land area is projected to have higher MAT and drying soil in the warm season in future scenarios, and both of these contribute to increases in the precipitation-limited area. To separate their exclusive contribution (MAT or PSSM), we fix one using the average of current prediction (2006 to 2015) and track the change in water-limited area due to the changes of the other (*Methods*). As expected, warming and drying land surface move most land areas toward the lower-right corner of the MAT-PSSM space, causing a regime shift from temperature-limited to precipitation-limited for some regions. These regime shifts are primarily due to a large increase in MAT, whose contribution is an order of magnitude larger than that due to PSSM (*SI Appendix*, Fig. S19). Although the predicted decrease in average soil moisture is prevalent in most models (39), its magnitude, after transformation using Eq. **1**, is relatively small compared with the temperature increase, which is global and large.

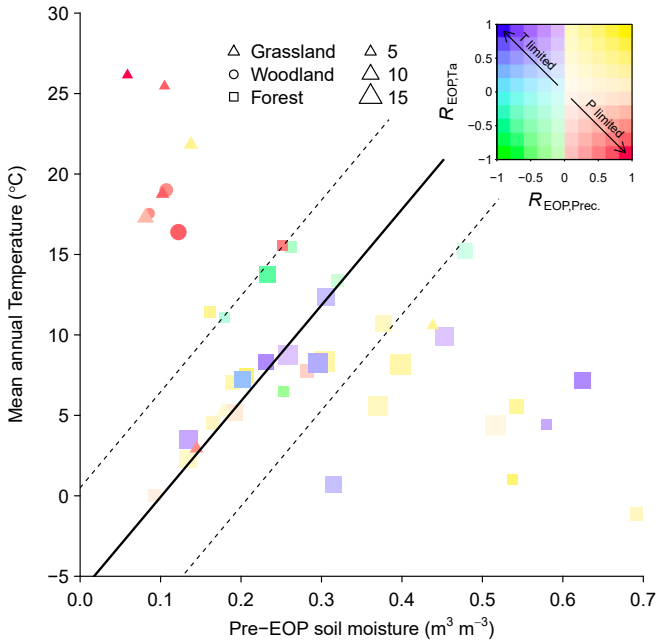

Fig. 3. Temperature and precipitation limitation for FLUXNET2015 sites. Correlation between EOP and air temperature (Ta) or precipitation (Prec.) in the 2D plain of MAT and PSSM from SMAP. The color indicates the EOP correlation with pre-EOP Ta and precipitation. The symbols represent different ecosystem types, with symbol sizes indicating number of years being used from each site. The solid and dashed black lines, which separate the precipitation-limited and temperature-limited regions, are adopted from Fig. 2.

In future projections, CO_2 fertilization may reduce stomatal conductance and increase water savings (35). This effect is considered in current Earth system models, but the prediction of vegetation growth varies enormously (40), making the total water usage uncertain. Additionally, most models do not include an explicit plant hydraulic model, leading to too large of a disconnection between SSM and root zone soil moisture (41). This suggests that simulated SSM in the upper 10 cm may not be as good a proxy for the root zone soil moisture as an observational proxy (where hydraulic redistribution is at play), and the contribution from the model PSSM might be underestimated. However, considering the low contribution from the soil moisture in determining the water-limited regions, our projected increase in water limitation on EOP should still be robust. Since this projection is made based on a fixed threshold obtained from space-for-time substitution, other factors affecting these relationships might emerge in the future, such as nutrient limitations and dynamic changes of biome types, contributing to the uncertainty of our analysis.

Due to the high interannual variability of precipitation, ecosystems limited by pre-EOP precipitation would experience large variations in EOP and consequently on ecosystem carbon uptake. These ecosystems will also be vulnerable to late growing-season high temperature and drought, which are projected to intensify in many regions with future warming (42, 43), further enhancing the interannual variability of terrestrial carbon uptake (44, 45). Considering the projected decrease of soil moisture during the late growing season (39), a decrease of late-season photosynthesis induced by strengthening moisture limitation may also be anticipated. Although our analysis does not include samples in tropical rainforests due to the low seasonality and inaccurate soil moisture satellite retrievals, previous studies suggest that water may play an important role in regulating leaf flushing during the dry season (46). Recent studies also suggest that the atmospheric CO_2 growth rate (CGR) is strongly coupled to the global terrestrial water storage and tropical land temperature (47) and that CGR sensitivity to tropical temperature has doubled due to the soil moisture decline in the past decades (48), further emphasizing the key role of moisture availability for carbon cycle, especially photosynthesis processes. The long-term declining trend and increasing variability of soil moisture in many regions may also reduce the capacity of continents to act as carbon sinks (15). Our study projects an increase in water-limited areal extent, mostly due to the increase in MAT, suggesting an even stronger impact of water availability on late-season carbon uptake in the future. The observed MAT and pre-EOP soil moisture regulation on EOP responses to environmental factors can also be used to constrain soil water stress on photosynthesis in Earth system models, reducing the uncertainties in future carbon cycle predictions.

Materials and Methods

CSIF Dataset. The CSIF dataset used in this study is a machine learning-generated, high-quality dataset with a 0.05° spatial and 4-d temporal resolution. This dataset first trained and validated a neural network (NN) using OCO-2 SIF and colocating MODIS MCD43C4 nadir bidirectional reflectance distribution function (BRDF)-adjusted reflectance during 2014 to 2017 (23). The NN was then used to generate the CSIF dataset using four bands (blue, green, red, and near-infrared) reflectance from MODIS for 2001 to 2017. Validation shows very high consistency with OCO-2 SIF (23). In this study, we used the clear-sky daily SIF, which shows stronger correlation with satellite observation and eddy covariance-estimated GPP (49). The 0.05° dataset was aggregated to 0.5° to match the resolution of other datasets. Since this dataset is not based on direct satellite SIF observations, justifications of using reflectance to predict SIF as well as potential caveats are discussed in detailed in *SI Appendix*, Text S1.

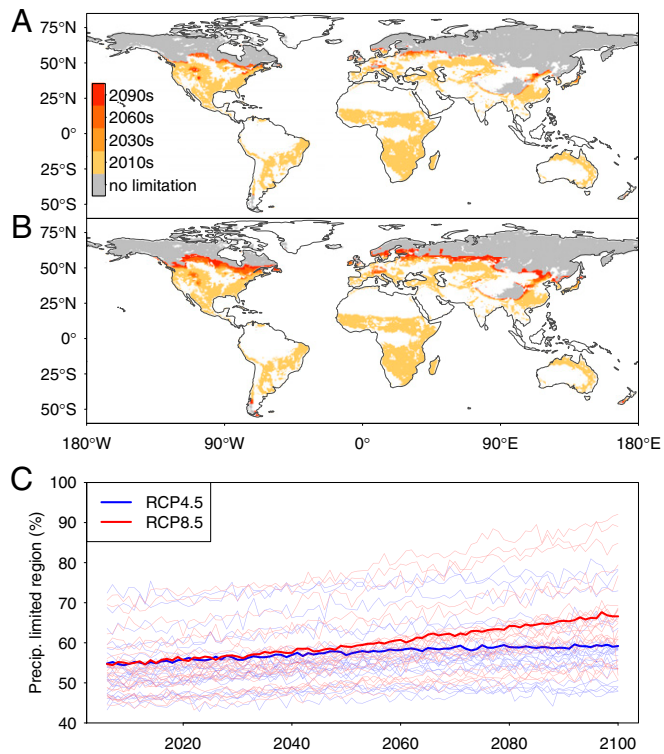

Fig. 4. Future prediction of regions with EOP limited by precipitation. Changes of future EOP limitation under RCP4.5 (*A*) and RCP8.5 (*B*) scenarios. (*C*) Changes of proportion of precipitation-limited regions to the total vegetated land (colored or gray area in *A* during 2006 to 2100). The thick lines indicate the multimodel ensemble median and each thin line represents prediction from individual models.

Climate Datasets. We used two types of climate dataset for the climate sensitivity of late-season photosynthesis analysis. The first type is from the ERA-Interim reanalysis data (50), air temperature at 2 m ("t2m"), total precipitation ("tp"), and photosynthetically active radiation ("par") were used. The second type is from remote sensing-based dataset: the MODIS land surface temperature (LST) from Aqua satellite (MYD11C2) (51), precipitation from the Global Precipitation Climatology Project (GPCP) (52), and PAR from Breathing Earth System Simulator (BESS) (53). Additionally, we also used the soil moisture retrievals from SMAP to get the preseason soil water condition (26). The detailed information for these datasets can be found in *SI Appendix*, Text S3.

FLUXNET2015 Dataset. We used the daily eddy covariance observations from the FLUXNET2015 Tier 1 dataset 54 to derive the EOP and analyze the temperature and precipitation limitation. Among the 166 Tier 1 sites, a rigorous data quality check and site (site-year) selection criteria are applied and described in *SI Appendix*, Text S4. We used the daily GPP estimates based on the nighttime partitioning method (55) and the reference Ustar ("GPP_NT_VUT_REF") to derive the EOP. For months with no valid net ecosystem exchange (NEE) observations (monthly mean "NEE_VUT_REF_QC" = 0, mostly in high latitude nongrowing season), GPP was set to 0 to avoid unrealistic GPP by the gap-filling algorithm. The MAT was calculated based on the site measured temperature. To be consistent with the CSIF analysis, we also calculated the PSSM using SMAP retrievals since not all sites have soil moisture observation and the measurement depth varies across sites. For the validation of the CSIF retrieved EOP, we further visually selected sites that were located in homogenous landscapes within 5 km × 5 km. This footprint size is comparable with the 0.05° CSIF resolution, so that their phenological dates are comparable. Altogether, 24 sites were used in this validation (*SI Appendix*, Table S2).

CMIP5 Models. We used 23 CMIP5 models to predict the future dynamic of the regions limited by precipitation or temperature (*SI Appendix*, Table S3). Both RCP4.5 and RCP8.5 scenarios were analyzed. To calculate the pre-EOP soil moisture, we first obtained the multiyear average EOP from CSIF. SSM ("mrsos") was then linearly interpolated to daily values and averaged over the 1-mo pre-EOP period. The soil depth representing SSM varies among models, but this difference is ignored here for simplicity. The model ensemble median for the water-limited regions was calculated from the multimodel median MAT and pre-EOP soil moisture using the SVM from remote sensing-based analysis.

Phenology Retrieval. We used a smoothing and threshold-based method to retrieve EOPs from both CSIF and EC-based GPP estimates (GPP_{EC}). This method has been previously used in other studies (56), and we improved it by using a weighted scheme to smooth the GPP_{EC} time series based on the data quality. First, the peak growing season was determined by the multiyear average monthly GPP or CSIF. If the peak of growing season is between April to September, the growing cycle starts from January and ends in December; otherwise, the sites or pixels may be located in the dry Mediterranean region or southern hemisphere, and the growing cycle starts from the previous May to current April. Second, with the growing cycle separated, the daily GPP_{EC} or 4-d CSIF data were smoothed using a weighted spline with 9 (for CSIF) or 11 (for GPP_{EC}) degrees of freedom. The weights were determined by the "NEE_VUT_REF_QC," which ranges from 0 to 1 and rescaled to 0.05 to 1, so that the GPP during polar night will be set to 0 and still have constraint on the smoothing curve. Third, using the multiyear-averaged smoothed GPP_{EC} or CSIF, the threshold for determining the EOP is calculated as the minimum + 30% of the amplitude. This site-specific fixed threshold is used to derive EOP for each site/pixel. If multiple peaks exist within 1 y, the EOP is extracted from the later one if the second photosynthetic active period (GPP > threshold) is greater than 30 d.

Analysis. With the multiyear average EOP, we calculated the average pre-EOP climate for each variable with different preseason length (15, 30, 60, 90 d). For variables with an 8-d temporal resolution (e.g., MODIS LST), they were linearly interpolated to daily values. The correlations or partial correlations were calculated for each preseason length, and the strongest correlation for each pixel or site was used to represent the pre-EOP climate limitations.

We used the SVM to separate the pixels with significant ($P < 0.1$) positive and negative correlations between pre-EOP climate and EOP. SVM is a widely used supervised learning method for classification problems (57). The labeled samples are first projected to a multidimensional (two for our case) space, with each dimension corresponding to one predictor variable. The essence of this algorithm is to find an optimum hyperplane (or line for our study) that separates the labeled samples into different categories, so that the distance between each category is maximized. The classification was conducted for temperature and precipitation separately using MAT and pre-EOP SM as predictors; positive and negative correlation between climate factors and EOP are the two groups that need to be separated. We also trained an SVM to separate the temperature-limited (positively correlated with air temperature) and water-limited (positively correlated with precipitation) pixels. Pixels limited by both or neither were removed from analysis (less than 10% of the total points). The resultant SVM is a function of both predictor variables and can be used to predict whether the EOP or late growing-season photosynthesis is limited by water or temperature. The "svm" function in the R package "e1071" (58) was used with a linear kernel. In addition to this classification method, we also compared another threshold-based method, as detailed in *SI Appendix*, Text S5.

To separate the contribution of increasing MAT and variations of SSM to the changes of water limitation on EOP using CMIP5 simulations, we set up two independent analyses that fix either MAT or pre-EOP SM using the average from the first 10 y of RCP prediction (2006 to 2015) and let the other change with time. The contribution of the MAT (β_{MAT}) and pre-EOP SM (β_{SM}) to the expansion of water-limited regions can be estimated using the equation below for each model and for the ensemble:

$$\beta = \frac{A_t^{fix}}{A_{2010s}} \quad \{t = 2010\text{s}, 2020\text{s}, \ldots\}, \qquad [1]$$

where A with a subscript represents the area of water-limited regions in that decade, and the superscript indicates that either MAT or pre-EOP SM is fixed, corresponding to β_{SM} and β_{MAT}, respectively.

Data Availability. The CSIF dataset used in the analysis can be accessed through https://figshare.com/articles/CSIF/6387494. Other datasets used in the analysis are also publicly available: BESS PAR, http://environment.snu.ac.kr/bess_rad/; MODIS LST, https://lpdaac.usgs.gov/products/myd11c2v006/; GPCP, https://catalog.data.gov/dataset/global-precipitation-climatology-project-gpcp-climate-data-record-cdr-version-1-3-daily; ERA-Interim, https://www.ecmwf.int/en/forecasts/datasets/reanalysis-datasets/era-interim; SMAP soil moisture, https://nsidc.org/data/SPL3SMP_E; FLUXNET2015, https://fluxnet.fluxdata.org/data/fluxnet2015-dataset/; and CMIP5, https://esgf-node.llnl.gov/search/cmip5/.

ACKNOWLEDGMENTS. We acknowledge all the principal investigators who contributed data to the FLUXNET Tier 1 dataset. We acknowledge the World Climate Research Programme's Working Group on Coupled Modelling, which is responsible for CMIP, and we thank the climate-modeling groups (listed in *SI Appendix*, Table S3) for producing and making available their model output. For CMIP, the US Department of Energy's Program for Climate Model Diagnosis and Intercomparison provides coordinating support and led development of software infrastructure in partnership with the Global Organization for Earth System Science Portals. We acknowledge comments by Dr. Shilong Piao on the early version of the manuscript. Y.Z. acknowledges funding from NASA Grant NNH16ZDA001N-AIST. P.G. acknowledges support from NASA Research Opportunities in Space and Earth Science Terrestrial Hydrology Grant NNH17ZDA00IN-THP and National Oceanic and Atmospheric Administration Modeling, Analysis, Predictions, and Projections Grant NA17OAR4310127. Portions of this research were carried out at the Jet Propulsion Laboratory, California Institute of Technology, under contract with NASA (80NM0018D0004). N.C.P. acknowledges support from the Earth Science Division Interdisciplinary Science Program (16-IDS16-0072). A.P.W. acknowledges funding from NASA Modeling, Analysis, and Prediction Program Grant 80NSSC17K0265.

1. Z. Zhu *et al*., Greening of the Earth and its drivers. *Nat. Clim. Chang.* **6**, 791–795 (2016).
2. C. Chen *et al*., China and India lead in greening of the world through land-use management. *Nat. Sustain.* **2**, 122–129 (2019).
3. R. Buitenwerf, L. Rose, S. I. Higgins, Three decades of multi-dimensional change in global leaf phenology. *Nat. Clim. Chang.* **5**, 364–368 (2015).
4. K. Huang *et al*., Enhanced peak growth of global vegetation and its key mechanisms. *Nat. Ecol. Evol.* **2**, 1897–1905 (2018).
5. C. Le Quéré *et al*., Global carbon budget 2017. *Earth Syst. Sci. Data* **10**, 405–448 (2018).
6. P. Friedlingstein *et al*., Uncertainties in CMIP5 climate projections due to carbon cycle feedbacks. *J. Clim.* **27**, 511–526 (2013).
7. T. Wang *et al*., Emerging negative impact of warming on summer carbon uptake in northern ecosystems. *Nat. Commun.* **9**, 5391 (2018).
8. J. Peñuelas *et al*., Shifting from a fertilization-dominated to a warming-dominated period. *Nat. Ecol. Evol.* **1**, 1438–1445 (2017).

9. Q. Liu *et al*., Delayed autumn phenology in the Northern Hemisphere is related to change in both climate and spring phenology. *Glob. Change Biol.* **22**, 3702–3711 (2016).
10. A. D. Richardson *et al*., Climate change, phenology, and phenological control of vegetation feedbacks to the climate system. *Agric. For. Meteorol.* **169**, 156–173 (2013).
11. X. Lian *et al*., Summer soil drying exacerbated by earlier spring greening of northern vegetation. *Sci. Adv.* **6**, eaax0255 (2020).
12. W. Buermann *et al*., Widespread seasonal compensation effects of spring warming on northern plant productivity. *Nature* **562**, 110–114 (2018).
13. S. Wolf *et al*., Warm spring reduced carbon cycle impact of the 2012 US summer drought. *Proc. Natl. Acad. Sci. U.S.A.* **113**, 5880–5885 (2016).
14. B. D. Stocker *et al*., Drought impacts on terrestrial primary production underestimated by satellite monitoring. *Nat. Geosci.* **12**, 264–270 (2019).
15. J. K. Green *et al*., Large influence of soil moisture on long-term terrestrial carbon uptake. *Nature* **565**, 476–479 (2019).
16. Y. Zhang *et al*., Canopy and physiological controls of GPP during drought and heat wave. *Geophys. Res. Lett.* **43**, 3325–3333 (2016).
17. A. A. Gitelson, M. N. Merzlyak, Remote estimation of chlorophyll content in higher plant leaves. *Int. J. Remote Sens.* **18**, 2691–2697 (1997).
18. X. Luo, H. Croft, J. M. Chen, L. He, T. F. Keenan, Improved estimates of global terrestrial photosynthesis using information on leaf chlorophyll content. *Glob. Change Biol.* **25**, 2499–2514 (2019).
19. Y. H. Fu *et al*., Declining global warming effects on the phenology of spring leaf unfolding. *Nature* **526**, 104–107 (2015).
20. Y. Sun *et al*., OCO-2 advances photosynthesis observation from space via solar-induced chlorophyll fluorescence. *Science* **358**, eaam5747 (2017).
21. A. Porcar-Castell *et al*., Linking chlorophyll a fluorescence to photosynthesis for remote sensing applications: Mechanisms and challenges. *J. Exp. Bot.* **65**, 4065–4095 (2014).
22. T. S. Magney *et al*., Mechanistic evidence for tracking the seasonality of photosynthesis with solar-induced fluorescence. *Proc. Natl. Acad. Sci. U.S.A.* **116**, 11640–11645 (2019).
23. Y. Zhang, J. Joiner, S. H. Alemohammad, S. Zhou, P. Gentine, A global spatially contiguous solar-induced fluorescence (CSIF) dataset using neural networks. *Biogeosciences* **15**, 5779–5800 (2018).
24. M. Huang *et al*., Air temperature optima of vegetation productivity across global biomes. *Nat. Ecol. Evol.* **3**, 772–779 (2019).
25. P. A. Dirmeyer, P. Gentine, M. B. Ek, G. Balsamo, "Land surface processes relevant to sub-seasonal to seasonal (S2S) prediction" in *Sub-Seasonal to Seasonal Prediction*, A. W. Robertson, F. Vitart, Eds. (Elsevier, 2019), pp. 165–181.
26. D. Entekhabi *et al*, SMAP Handbook–Soil Moisture Active Passive: Mapping Soil Moisture and Freeze/Thaw from Space (2014). https://smap.jpl.nasa.gov/system/internal_resources/details/original/178_SMAP_Handbook_FINAL_1_JULY_2014_Web.pdf. Accessed 20 March 2019.
27. R. B. Neumann, Z. G. Cardon, The magnitude of hydraulic redistribution by plant roots: A review and synthesis of empirical and modeling studies. *New Phytol.* **194**, 337–352 (2012).
28. S. Walther *et al*., Satellite observations of the contrasting response of trees and grasses to variations in water availability. *Geophys. Res. Lett.* **46**, 1429–1440 (2019).
29. A. J. Teuling *et al*., Contrasting response of European forest and grassland energy exchange to heatwaves. *Nat. Geosci.* **3**, 722–727 (2010).
30. H. J. De Boeck, S. Bassin, M. Verlinden, M. Zeiter, E. Hiltbrunner, Simulated heat waves affected alpine grassland only in combination with drought. *New Phytol.* **209**, 531–541 (2016).
31. E. Cremonese *et al*., Heat wave hinders green wave: The impact of climate extreme on the phenology of a mountain grassland. *Agric. For. Meteorol.* **247**, 320–330 (2017).
32. G. R. Quetin, A. L. S. Swann, Empirically derived sensitivity of vegetation to climate across global gradients of temperature and precipitation. *J. Clim.* **30**, 5835–5849 (2017).
33. K. A. Novick *et al*., The increasing importance of atmospheric demand for ecosystem water and carbon fluxes. *Nat. Clim. Chang.* **6**, 1023–1027 (2016).
34. P. B. Reich *et al*., Effects of climate warming on photosynthesis in boreal tree species depend on soil moisture. *Nature* **562**, 263–267 (2018).
35. L. Lemordant, P. Gentine, M. Stéfanon, P. Drobinski, S. Fatichi, Modification of land-atmosphere interactions by CO2 effects: Implications for summer dryness and heat wave amplitude. *Geophys. Res. Lett.* **43**, 10,240–10,248 (2016).
36. Y. Yang, M. L. Roderick, S. Zhang, T. R. McVicar, R. J. Donohue, Hydrologic implications of vegetation response to elevated CO 2 in climate projections. *Nat. Clim. Chang.* **9**, 44–48 (2019).
37. S. B. Gray *et al*., Intensifying drought eliminates the expected benefits of elevated carbon dioxide for soybean. *Nat. Plants* **2**, 16132 (2016).
38. W. A. Obermeier *et al*., Reduced CO_2 fertilization effect in temperate C3 grasslands under more extreme weather conditions. *Nat. Clim. Chang.* **7**, 137–141 (2017).
39. A. Berg, J. Sheffield, P. C. D. Milly, Divergent surface and total soil moisture projections under global warming. *Geophys. Res. Lett.* **44**, 236–244 (2017).
40. A. Ahlström, G. Schurgers, A. Arneth, B. Smith, Robustness and uncertainty in terrestrial ecosystem carbon response to CMIP5 climate change projections. *Environ. Res. Lett.* **7**, 044008 (2012).
41. D. Kennedy *et al*., Implementing plant hydraulics in the community land model, version 5. *J. Adv. Model. Earth Syst.* **11**, 485–513 (2019).
42. A. Dai, Increasing drought under global warming in observations and models. *Nat. Clim. Chang.* **3**, 52–58 (2012).
43. A. P. Williams *et al*., Temperature as a potent driver of regional forest drought stress and tree mortality. *Nat. Clim. Chang.* **3**, 292–297 (2012).
44. A. Ahlström *et al*., Carbon cycle. The dominant role of semi-arid ecosystems in the trend and variability of the land CO_2 sink. *Science* **348**, 895–899 (2015).
45. S. Zhou, Projected increases in intensity, frequency, and terrestrial carbon costs of compound drought and aridity events. *Science Advances* **5** (1):), eaau5740, 10.1126/sciadv.aau5740 (2019).
46. K. Guan *et al*., Photosynthetic seasonality of global tropical forests constrained by hydroclimate. *Nat. Geosci.* **8**, 284–289 (2015).
47. V. Humphrey *et al*., Sensitivity of atmospheric CO_2 growth rate to observed changes in terrestrial water storage. *Nature* **560**, 628–631 (2018).
48. X. Wang *et al*., A two-fold increase of carbon cycle sensitivity to tropical temperature variations. *Nature* **506**, 212–215 (2014).
49. Y. Zhang *et al*., On the relationship between sub-daily instantaneous and daily total gross primary production: Implications for interpreting satellite-based SIF retrievals. *Remote Sens. Environ.* **205**, 276–289 (2018).
50. P. Berrisford *et al*, The ERA-Interim Archive (Version 2.0, European Centre for Medium-Range Weather Forecasts, 2011). https://www.ecmwf.int/file/21498/download?token=cr31Wrx8. Accessed 22 March 2019.
51. Z. Wan, MYD11A2 MODIS/Aqua land surface temperature/emissivity 8-Day L3 global 1 km SIN grid V006 (2015). https:/doi.org/10.5067/MODIS/MYD11A2.006. Accessed 7 March 2019.
52. G. J. Huffman *et al*., The Global Precipitation Climatology Project (GPCP) combined precipitation dataset. *Bull. Am. Meteorol. Soc.* **78**, 5–20 (1997).
53. Y. Ryu, C. Jiang, H. Kobayashi, M. Detto, MODIS-derived global land products of shortwave radiation and diffuse and total photosynthetically active radiation at 5 km resolution from 2000. *Remote Sens. Environ.* **204**, 812–825 (2018).
54. G. Z. Pastorello *et al*., A New Data Set to Keep a Sharper Eye on Land-Air Exchanges. *Eos* **98**, https://doi.org/10.1029/2017EO071597 (2017).
55. M. Reichstein *et al*., On the separation of net ecosystem exchange into assimilation and ecosystem respiration: Review and improved algorithm. *Glob. Change Biol.* **11**, 1424–1439 (2005).
56. T. F. Keenan *et al*., Net carbon uptake has increased through warming-induced changes in temperate forest phenology. *Nat. Clim. Chang.* **4**, 598–604 (2014).
57. J. A. K. Suykens, J. Vandewalle, Least squares support vector machine classifiers. *Neural Process. Lett.* **9**, 293–300 (1999).
58. D. Meyer, Support vector machines. The interface to libsvm in package e1071 (2017). https://cran.r-project.org/web/packages/e1071/vignettes/svmdoc.pdf. Accessed 27 March 2020.